Ceramics International 47 (2021) 29363–29370

Contents lists available at ScienceDirect

Ceramics International

journal homepage: www.elsevier.com/locate/ceramint

Femtosecond laser generation of bimetallic oxide nanoparticles with potential X-ray absorbing and magnetic functionalities for medical imaging applications

Aida Naghilou [a,b,*], Oscar Bomati-Miguel [a,c,**], Ana Subotic [a], Ruth Lahoz [d], Markus Kitzler-Zeiler [e], Christine Radtke [b], Miguel A. Rodríguez [f], Wolfgang Kautek [a]

[a] Department of Physical Chemistry, University of Vienna, Vienna, Austria
[b] Department of Plastic, Reconstructive, and Aesthetic Surgery, Medical University of Vienna, Vienna, Austria
[c] Departamento de Física de La Materia Condensada and Institute of Research on Electron Microscopy and Materials (IMEYMAT), Universidad de Cádiz, Puerto Real (Cádiz), Spain
[d] Instituto de Nanociencia y Materiales de Aragón (CSIC-University of Zaragoza), Zaragoza, Spain
[e] Photonics Institute, Technische Universität Wien, Vienna, Austria
[f] Instituto de Cerámica y Vidrio (CSIC), Madrid, Spain

ARTICLE INFO

Keywords:
Binary oxides ceramics
Laser ablation in liquid
Bimetallic nanoparticles
Laser ablation threshold
Laser ablation synthesis in solutions

ABSTRACT

Bimetallic nanoparticles have gained vivid attention due to their unique and synergistic properties. They can be used in fields such as solar cells, optics, sensing, as well as medicine. The generation of bimetallic nanoparticles, containing oxide phases of both magnetic and X-ray attenuating metals for bioimaging applications has been challenging with traditional chemical synthesis methods. An alternative is the generation of nanoparticles from binary oxide ceramics by laser ablation in liquid. However, the applicability of this technique for production of hybrid nanoparticles consisting of magnetic and X-ray absorbing elements has not been demonstrated yet.

In this work, novel ceramics composed of bimetallic oxide phases of iron-tantalum, iron-tungsten, and iron-bismuth were produced by a reaction-sintering method. The bulk samples were characterized with scanning electron microscopy, energy dispersive X-ray spectroscopy, and X-ray diffractometry. Nanoparticles were produced in aqueous and ethanol solutions by employing a femtosecond laser and characterized with transmission electron microscopy, selected area electron diffraction, and energy dispersive X-ray spectroscopy. The results demonstrated that the production of binary oxide bulk ceramics and their subsequent laser ablation in liquids leads to the successful generation of bimetallic oxide nanoparticles, without a core-shell morphology. In addition, it was found that the ablation threshold fluence of bulk samples as well as the crystallinity of the synthesized nanoparticles is governed by both the nature of the metallic oxide ceramics and the employed liquid. The results pave the way for a single step generation of well-defined bimetallic nanoparticles by laser ablation that could potentially exhibit X-ray and magnetic absorption properties suitable for multimodal imaging applications.

1. Introduction

Nanoparticles (NPs) have become a ubiquitous part of modern science and technology in fields such as catalysis, optics, plasmonic, and biotechnology [1–4]. Bimetallic NPs are of special interest as they blend the tunable properties of their constituents, greatly expanding their application range [5,6]. This synergistic characteristic of the bimetallic NPs has made them attractive for (electro-)catalysis, analytics, supercapacitors, green energy, and sensing [7–13]. The biomedical applications of bimetallic NPs have also been under investigation. Copper-silver NPs

Abbreviations: at.%, Atomic percentage; CE-MRI, Contrast enhanced magnetic resonance imaging; EDX, Energy dispersive X-ray spectroscopy; LASiS, Laser ablation synthesis in solution; ME, High atomic number metals; MRI, Magnetic resonance imaging; NP, Nanoparticle; SAED, Selected area electron diffraction; SEM, Scanning electron microscopys; TEM, Transmission electron microscopy; XRD, X-ray diffractometry.

* Corresponding author. Department of Physical Chemistry, University of Vienna, Vienna, Austria.
** Corresponding author. Department of Physical Chemistry, University of Vienna, Vienna, Austria.
E-mail addresses: aida.naghilou@meduniwien.ac.at (A. Naghilou), oscar.bomati@uca.es (O. Bomati-Miguel).

https://doi.org/10.1016/j.ceramint.2021.07.103
Received 21 May 2021; Received in revised form 10 July 2021; Accepted 12 July 2021
Available online 13 July 2021

have been used for their antimicrobial effects [14], while gold-palladium NPs show potential in photothermal cancer therapy [15]. In addition, bimetallic NPs can be used as contrast agents in multimodal imaging, which enables an early-stage diagnosis of cancerous tissue, reducing the mortality rate, and greatly improving the patient's quality of life [16–24]. Among various multimodal imaging methods, simultaneous use of X-ray techniques (such as computed tomography and digital mammography) with magnetic resonance imaging (MRI) and contrast enhanced-MRI (CE-MRI) resulted in unique diagnostics properties [25]. This has led to the development of bimetallic NPs capable of combining a magnetic response and a high X-ray absorption coefficient [26–31]. Moreover, these hybrid NPs necessitate a high emission signal, high specificity, low cost, and high biocompatibility [32–34].

Iron oxide NPs especially maghemite (γ-Fe_2O_3) and magnetite (Fe_3O_4), are amongst the most widely studied biocompatible and biodegradable nanomaterials with magnetic properties [35–41]. NPs generated from metals with high atomic numbers such as gold [42,43], bismuth [44,45], tungsten [46], tantalum [47], and ytterbium [45,48] are examples of materials with X-ray attenuating applications [49,50]. Therefore, their combination with iron oxide NPs can lead to bimetallic NPs suitable for multimodal imaging applications.

Various chemical approaches have been utilized to produce bimetallic NPs which integrate iron oxide with X-ray attenuating elements [27–31]. The incorporation of bismuth in the core of iron oxide NP was shown to support the magnetic contrast and a strong X-ray attenuation [51]. However, it has been demonstrated that during conventional chemical synthesis, bismuth may fail to enter the iron oxide lattice and bonds on the surface of nanoparticles similar to surfactants [29,30]. This core-shell morphology without lattice incorporation was also reported for the combination of iron oxide with Ta_2O_5 [52]. In addition, chemical methods mostly require expensive and/or toxic precursors as well as controlled atmospheres and often fail to be transferred from the laboratory scale to industrial production [1,53,54]. Wet-chemical synthesis also requires long purification steps [55]. Hence, an alternative method for the successful production of well-defined, sustainable, and waste-free hybrid NPs is of great interest.

A promising technique for the generation of oxide bimetallic NPs is laser ablation synthesis in solutions (LASiS) [56,57]. This is a cost-effective, simple, environmentally friendly, and single step method, where the NPs are synthesized directly in a liquid medium without contaminations and byproducts [58]. The successful large and industrial scale production of NPs with this method has also been established and productivities in the order of grams per hour are achievable [59,60]. The productivity of the NP generation is heavily driven by the ablation mechanism. Hence, as the nature of the target and the liquid, the laser parameters, as well as the surface morphology greatly determine the laser ablation process, they affect the productivity [61–65]. The ablation rate increases almost linearly with pulse energy, laser beam area at a given fluence, and pulse numbers [54]. However, there is a certain limitation based on the expansion lifetime of the cavitation bubble, as it can scatter the next pulse and reduce the energies reaching the target surface [56,66]. The NP properties such as size, shape, composition, crystallinity, and morphology can also be controlled based on the quality of ablation targets, the liquid medium, and the laser parameters [54,59,64–69].

In this work, the fabrication of hybrid bimetallic NPs with LASiS is demonstrated. Ceramic targets incorporating a magnetic iron oxide, and an oxide phase of a high atomic number metal (Ta, W, and Bi) are produced by a reaction-sintering method. These combine magnetic and X-ray attenuation potentials. NPs generated from the bulk samples by femtosecond laser ablation in water and ethanol are studied. Characterization of the bulk material and NPs focuses on morphology, composition, and crystallinity.

2. Materials and methods

2.1. Bulk ceramic production

In order to enable the incorporation of metallic elements with high atomic numbers in the iron oxide lattice, samples consisting of binary oxide phases were produced. A ceramic reaction-sintering method was employed, and commercial iron oxide powders were weighed and mixed with powdered oxide phases of Ta_2O_5, WO_3, and Bi_2O_3 to obtain the stoichiometric phases $FeTaO_4$, Fe_2WO_6, and $FeBiO_3$ based on the corresponding phase equilibrium diagrams [70–74]. The resulting samples are denoted as Fe–Ta (iron-tantalum oxide ceramic), Fe–W (iron--tungsten oxide ceramic), and Fe–Bi (iron-bismuth oxide ceramic). These mixtures were processed by attrition milling (Y_2O_3 stabilized ZrO_2, 1 mm diameter balls) for 2 h to decrease the particle size and homogenize the composition. Then, cylindrical bulk samples (10 mm in height and 15 mm in diameter) were obtained via a biaxial pressing at 100 MPa. The obtained samples were thermal treated in a laboratory furnace at air with a 10 °C/min heating rate and 2 h of dwell time. After a few trials in order to reach almost completely oxide reactions, the selected reaction-sintering temperatures were chosen as 1400 °C, 1050 °C, and 750 °C, for Fe–Ta, Fe–W, and Fe–Bi, respectively. The obtained materials were characterized by X-ray diffractometry (XRD; Bruker D8-advanced with a LYNXEYE Si-strip detector) to determine the phases. XRD patterns were recorded from 10° to 70° (2θ) with a measurement time of 60 min. In addition, scanning electron microscopy (SEM; Zeiss Supra 55 VP) coupled with energy dispersive X-ray spectroscopy (EDX) were employed for characterization of microstructure and composition, respectively. Nine EDX spectra at various sites of the bulk samples were recorded and the quantitative results were averaged and presented in atomic percent (at.%).

2.2. Laser threshold fluence determination

An amplified Ti:Sapphire laser system delivering sub-30 fs pulses at a repetition rate of 5 kHz centered at 790 nm was employed. The bulk samples were positioned in a liquid cell and the beam was coupled in horizontally into the cell via a sapphire window. A custom optical system was used for focus determination [75]. The bulk ceramics were placed inside the cell filled with water or ethanol solutions with 0.5% citric acid. Citric acid helps to form a stable dispersion of NPs and has been shown to stabilize an aqueous dispersion of magnetite NPs [76]. For the threshold fluence (F_{th}) determination, the D^2-ln$F$ technique was used [77,78]. Here D is the width of the ablated areas measured by an optical microscope (Olympus STM-MJS) and F is the laser fluence calculated with:

$$F = \frac{2E}{w^2 \pi}$$

where E is the incident laser energy and w is the beam waist radius. w was determined by the knife edge method [79] in air to be (10.5 ± 0.1) μm. This value was corrected based on the refraction by the window and the liquid. E was also measured in air and the energy reaching the surface of the sample was calculated based on the reflection and absorption losses of the sapphire window and the liquid. For the calculation of F, the corrected beam radii and energies were employed. The bulk ceramic samples were scanned at various fluences at a constant scanning velocity of 0.1 mm/s corresponding to $N = 1206$ overlapping pulses for water and $N = 1221$ in ethanol based on the different beam radii in the two liquids.

2.3. Nanoparticle production

NPs were produced by irradiating the bulk ceramics in a meander scanning mode at a constant velocity of 0.1 mm/s. Deionized water plus

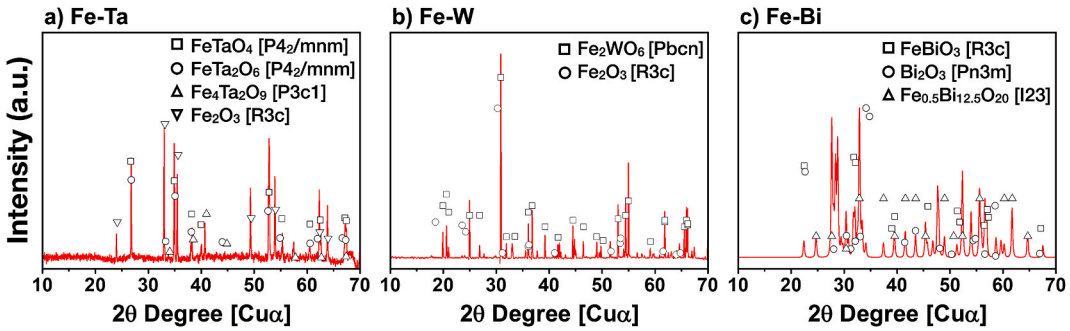

Fig. 1. XRD analysis of binary metal oxide bulk ceramics. a) Fe–Ta, b) Fe–W and c) Fe–Bi.

Table 1
EDX analysis results of the elemental composition of binary metal oxide bulk ceramics. Atomic percentages (at.%) and ratios are shown. ME: high atomic number metals (Ta, W, or Bi).

	Fe (at.%)	O (at.%)	Ta (at.%)	W (at.%)	Bi (at.%)	ME/Fe	O/(ME + Fe)
Fe–Ta	11 ± 3	70 ± 2	18 ± 2	–	–	1.7 ± 0.4	2.4 ± 0.3
Fe–W	19 ± 2	70 ± 3	–	11 ± 1	–	0.6 ± 0.1	2.4 ± 0.2
Fe–Bi	7 ± 3	82 ± 7	–	–	10 ± 4	1.4 ± 0.8	4.7 ± 1.4

0.5% citric acid as dispersant agent and ethanol (absolute, Sigma Aldrich) plus 0.5% citric acid were used. The laser pulse energy at the surface of the sample for NP generation was adjusted to 3.90 J cm^{-2} for the aqueous solution and 3.77 J cm^{-2} for the ethanol solution. The NPs were characterized by transmission electron microscopy (TEM; Philips CM200 TEM, LaB_6 cathode, 200 kV acceleration voltage), together with selected area electron diffraction (SAED), and EDX. A small amount of the colloidal specimen was placed on a carbon-coated copper grid and the solution was evaporated at room temperature.

3. Results and discussion

3.1. Characterization of bulk samples

Firstly, the produced ceramic materials were characterized to reveal the successful production of binary metal oxide phases. Based on the XRD results of the Fe–Ta sample (Fig. 1a), the presence of various crystalline phases was identified: three iron-tantalum oxide phases, $FeTaO_4$ and $FeTa_2O_6$, with tetragonal symmetry [$P4_2/mnm$] as the majority, and $Fe_4Ta_2O_9$ as additional phase with trigonal symmetry [P3c1] were present. Peaks also corresponded to the iron oxide phase hematite (α-Fe_2O_3), which could be an indication that a small fraction of the original iron oxide precursor has not reacted with the tantalum oxide. The XRD pattern of the Fe–W oxide ceramic (Fig. 1b) revealed the presence of crystalline Fe_2WO_6 phases with orthorhombic symmetry [Pbcn] and a small amount of Fe_2O_3 phase with a trigonal symmetry [R3c]. For Fe–Bi, a $FeBiO_3$ phase with trigonal symmetry [R3c] and two additional cubic phases of Bi_2O_3 [Pn3m] and $Fe_{0.5}Bi_{12.5}O_{20}$ [I23] were visible (Fig. 1c). These results confirmed the production of binary metal oxide ceramics.

The presence of multiple oxide phases, as seen from the XRD results, give rise to the elemental compositions shown in Table 1 and measured by EDX. The averages and standard deviations of the compositions as well as ratios of the high atomic number metals to Fe (ME/Fe) and oxygen to the metals, O/(ME + Fe) are also presented. The presence of various phases can be explained by the solid-state synthesis of the samples, leading to large diffusion paths and the generation of intermediate phases. Additionally, segregation during the sintering process of the sample preparation may occur [80], which could lead to higher inhomogeneities. The observed iron oxide phases as seen in the XRD results also support this interpretation. The oxygen contents measured in EDX have a larger incertitude as they may have been affected by the production process of the bulk samples and/or their thermal treatment, handling, and storage in air.

SEM micrographs revealed prominent variations between the material topography. Fe–Ta (Fig. 2a) showed a rather smooth morphology with featureless regions in comparison to the other samples. Fe–W (Fig. 2b) contained larger inhomogeneities in the form of surface defects, cracks, and pores. On the Fe–Bi bulk sample (Fig. 2c), a rough surface topography was observed, which could be related to a possible lack of densification during production.

3.2. Laser ablation behavior

The D^2-ln$F$ results are shown in Fig. 3a–c for Fe–Ta, Fe–W, and Fe–Bi respectively. As expected, the diameter of the ablated areas increases at higher incident fluences. The experimental data points are fitted with the D^2-ln$F$ model, and the fluence at which the width of the ablated area falls to zero, i.e. $D(F) = 0$ is defined as F_{th}.

The results of F_{th} determination are depicted in Fig. 4. F_{th} was found to be larger for ablation under ethanol in comparison to water for all samples. This is in line with previous experiments on Fe samples at similar pulse numbers [64], where the higher F_{th} was related to the plasma-induced dissociation of ethanol, facilitating the formation of solid carbon particles and longer hydrocarbon molecules which absorb part of the laser radiation and decrease the beam intensity reaching the sample surface [81,82]. The values of F_{th} for Fe–Ta are clearly greater in both liquid environments in comparison to the other two samples. Fe–W in turn also shows a higher F_{th} than Fe–Bi. This trend of decreasing F_{th} can be well explained based on the morphology of the bulk samples as seen in Fig. 2: While Fe–Ta has the smoothest morphology, Fe–W shows a certain density of surface defects, which are even more present on the Fe–Bi sample. Intrinsic surface defects have been well studied and contribute greatly to a higher absorption of laser pulses and decreasing F_{th} values [83–88]. This is in line with the results visible in Fig. 4.

3.3. Characterization of synthesized NPs

The targets were ablated in 0.5% citric acid aqueous and ethanol solutions and the generated NPs were characterized based on their

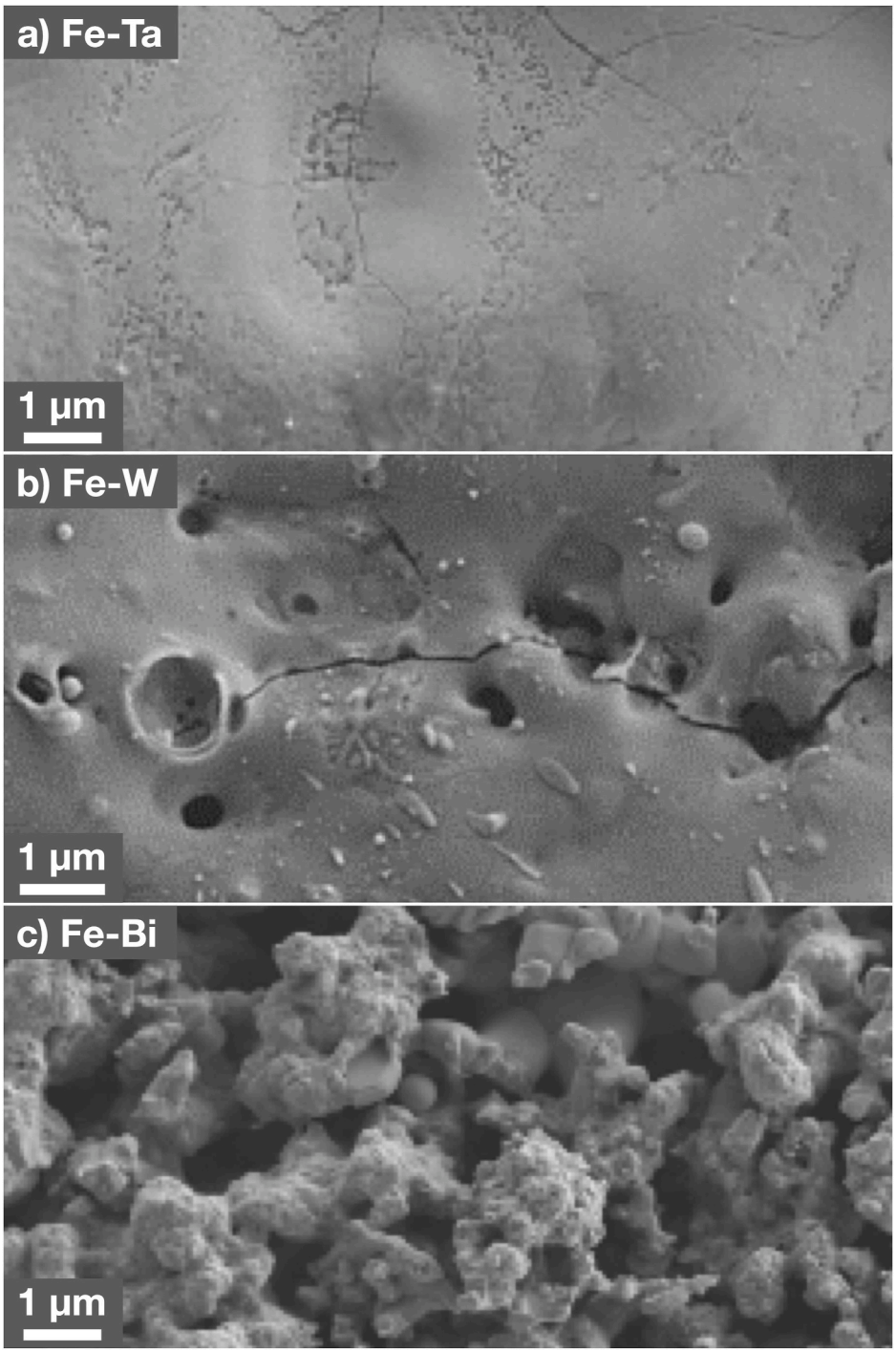

Fig. 2. SEM images of binary metal oxide bulk ceramics. a) Fe–Ta b) Fe–W and c) Fe–Bi.

composition to determine the formation of bimetallic oxides. It has been shown that the crystallinity of the NPs affects their magnetic properties for CE-MRI [89,90]. Thus, attention was also given to the crystalline structure of the NPs. In addition, it is well known that the size and diameter distribution of NPs depends on scan speed (irradiation duration) and pulse energy [54,59,64,68]. Hence, the scan speed and fluence were kept constant in these experiments to allow the direct evaluation of the influence of bulk sample and liquid nature on the synthesized NPs.

Fig. 5 and Fig. 6 show TEM micrographs and SAED patterns of NPs from the Fe–Ta, Fe–W and Fe–Bi samples produced in 0.5% citric acid aqueous and ethanol solutions, respectively. The arrows show the area, where the SAED data has been acquired. In water, Fe–Ta particles (Fig. 5a) showed a spherical morphology without chain formation or aggregation. SAED images indicated amorphous states. In contrast, The Fe–W NPs exhibited shapes deviating from spherical (Fig. 5b) with SAED patterns demonstrating their crystallinity. This was also observed for Fe–Bi (Fig. 5c), where the SAED data demonstrated crystalline particles.

TEM micrographs of Fe–Ta particles (Fig. 6a) produced in 0.5% citric acid ethanol solution showed a spherical morphology and amorphous states. For Fe–W, even though some smaller crystalline NPs were detected, most of the particles were larger, spherically shaped, and amorphous in both inner and outer areas (Fig. 6b). In contrast, both the

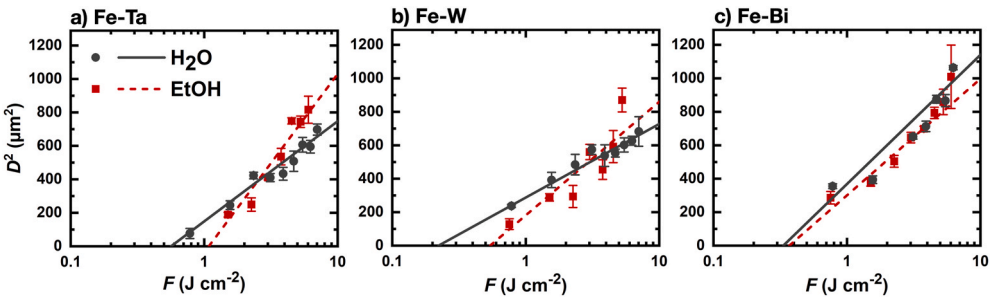

Fig. 3. The squared diameters of the ablated areas for various incident fluences fitted with the D^2-ln$F$ equation (lines) for a) Fe–Ta b) Fe–W c) Fe–Bi binary metal oxide bulk samples in 0.5% citric acid aqueous (grey circles, solid line) and ethanol solution (red squares, dashed line). (For interpretation of the references to colour in this figure legend, the reader is referred to the Web version of this article.)

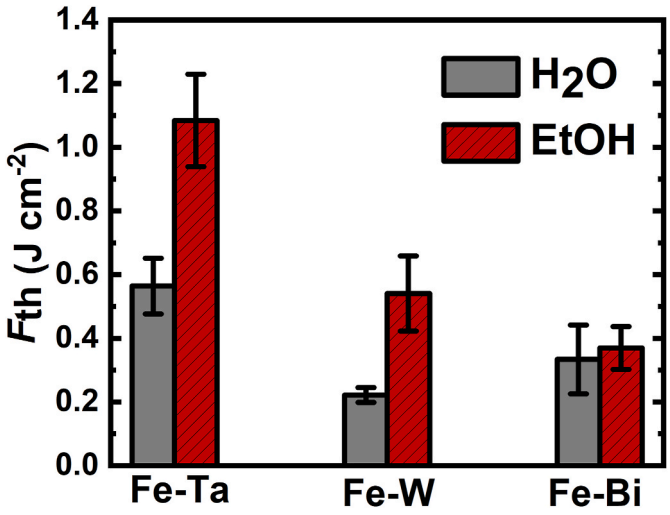

Fig. 4. F_{th} deduced from the D^2-ln$F$ data for experiments on Fe–Ta, Fe–W, and Fe–Bi binary metal oxide bulk ceramics in 0.5% citric acid aqueous (grey solid columns) and ethanol solution (red striped columns). (For interpretation of the references to colour in this figure legend, the reader is referred to the Web version of this article.)

larger and smaller NPs produced from the Fe–Bi bulk sample exhibited crystallinity in ethanol (Fig. 6c).

Unlike previous studies of hybrid NP production with chemical approaches, where Bi and Ta oxides were described as bonding on the surface of iron oxide NPs [30,51,52], no core-shell morphology was observed. In addition, EDX measurements on NPs was employed to analyze their compositions. For larger NPs, multiple EDX measurements in the middle as well as the outer areas were measured as shown in one example in Fig. 6b. The average results are shown in Table 2. This indicated the successful presence of both Fe, as well as Ta, W, or Bi in the laser synthesized NPs. This is crucial since the incorporation of high atomic number element in the iron oxide lattice has been shown to yield NPs suitable for MRI and X-ray imaging [51].

The ratio of elements in the NPs was compared to that of the bulk ceramics (Fig. 7). For the experiments in water, the ratio of Ta/Fe increased in the NPs, which could be due to the loss of Fe during the NP production process. This excess was even greater during experiments in ethanol. EDX analysis also indicated an increase of the O/(Ta + Fe) ratio from the bulk sample to NPs (Fig. 7a) in water, but not in ethanol. Similar metal stoichiometry of W/Fe in the NPs and the bulk sample were detected in both water and ethanol. Oxygen, however, was lost in the NP generation process (Fig. 7b). The NPs synthesized from the Fe–Bi sample resulted in a similar Bi/Fe ratio as that of the bulk material and a reduced oxygen composition (Fig. 7c). The observed oxygen losses between the bulk samples and the NPs in both liquids may be related to the reductive property of the laser plasma containing partially ionized bulk sample material and free electrons in the confined bubble volume at the solid-liquid interface [91–93].

Overall, all LASiS synthesized NPs showed the successful presence of bimetallic oxide phases. Their composition and crystallinity were found to be dependent on the ceramic sample and the liquid. NPs of Fe–Ta showed the largest ME/Fe composition variations from the bulk material and were amorphous in both water and ethanol, while NPs of Fe–W and Fe–Bi had a more similar ME/Fe composition to their respective bulk

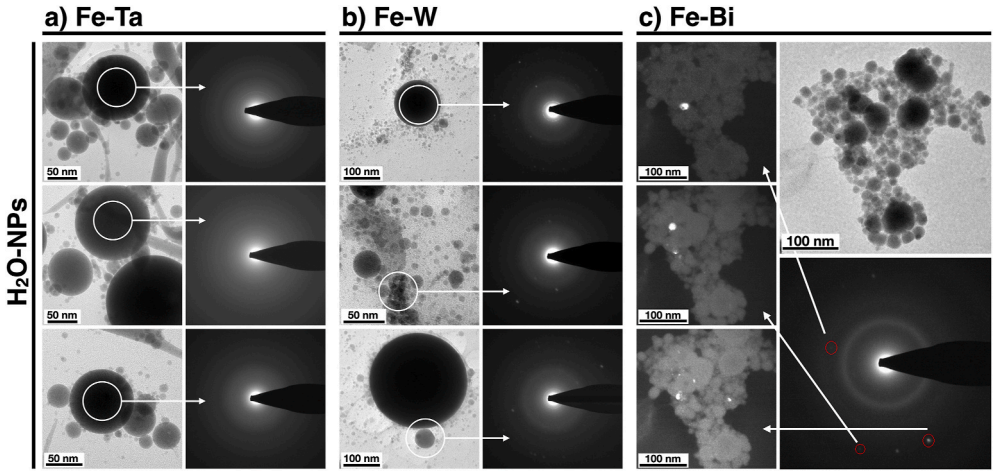

Fig. 5. TEM and SAED patterns of NPs produced in 0.5% citric acid aqueous solution from a) Fe–Ta b) Fe–W c) Fe–Bi binary metal oxide bulk ceramics. NPs were produced at $N = 1206$ pulse overlap and $F = 3.90$ J cm^{-2}.

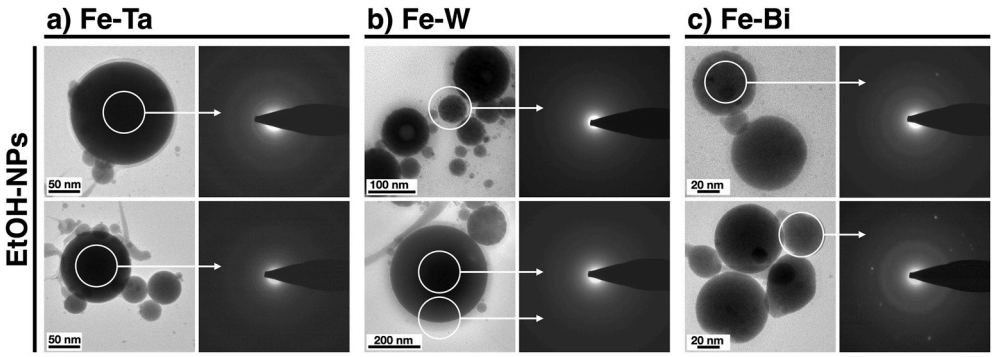

Fig. 6. TEM and SAED patterns of NPs produced in 0.5% citric acid ethanol solution a) Fe–Ta b) Fe–W c) Fe–Bi binary metal oxide ceramics. NPs were produced at $N = 1221$ pulse overlap and $F = 3.77$ J cm^{-2} fluence.

Table 2
EDX analysis results of the elemental composition of the NPs synthesized in water and ethanol.

		Fe (at.%)	O (at.%)	Ta (at.%)	W (at.%)	Bi (at.%)
H_2O	Fe–Ta	5 ± 1	75 ± 4	20 ± 3	–	–
	Fe–W	27 ± 4	54 ± 5	–	18 ± 2	–
	Fe–Bi	10 ± 3	76 ± 4	–	–	14 ± 2
EtOH	Fe–Ta	5 ± 2	70 ± 5	25 ± 4	–	–
	Fe–W	30 + 2	51 ± 2	–	19 ± 2	–
	Fe–Bi	13 ± 3	72 ± 4	–	–	15 ± 1

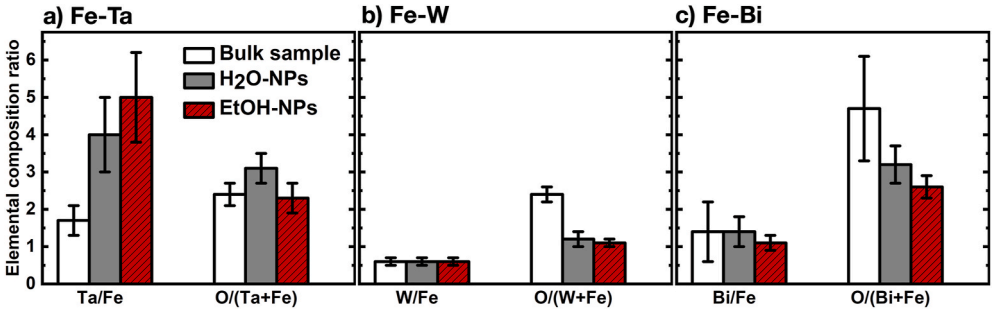

Fig. 7. Comparison of elemental composition ratios based on the at.% of bulk samples (white columns) and NPs produced in 0.5% citric acid aqueous (grey solid columns) and ethanol solution (red striped columns) measured by EDX and shown in Tables 1 and 2, respectively.

sample. As the crystallinity of iron oxide NPs is an essential factor for their success in CE-MRI applications [89,90], the Fe–W NPs generated in water and the Fe–Bi NPs synthesized in both water and ethanol could be taken into consideration and after large-scale production, further investigated for their applicability as multimodal contrast agents. NPs synthesized by LASiS are well-known to be tunable by the ablation target morphology, liquid properties, and laser parameters. Hence, further investigations using the ceramics and laser ablation method demonstrated here could enable a targeted production of hybrid NPs with desired size, composition, and crystallinity for multimodal imaging.

4. Conclusions

In this work, the generation of hybrid NPs combining the oxide phases of magnetic and high atomic number metallic elements with LASiS was demonstrated. Novel ceramic targets from magnetic iron oxide and an oxide phase of Ta, W, and Bi were produced by a reaction-sintering method. XRD results confirmed the presence of bimetallic oxide phases. In addition, the bulk ceramics varied in their surface morphology. Fe–Ta showed a smooth surface, while Fe–W contained surface defects and Fe–Bi had the highest inhomogeneity. This increasing density of surface defects was in line with the laser ablation experiments, where the onset of ablation, F_{th}, decreased as the inhomogeneity increased.

The ceramic materials were used as laser targets for the generation of NPs in aqueous and ethanol solutions with citric acid. While the NPs from Fe–Ta were amorphous in both water and ethanol, the Fe–Bi NPs generated in both liquids showed crystallinity. Interestingly, only the Fe–W NPs were affected by the liquid and were crystalline in water and mostly amorphous in ethanol. The synthesized NPs were comprised of bimetallic oxide phases and showed the presence of both Fe and the high atomic number metals of the respective samples without a core-shell morphology. These results demonstrated that fs-laser synthesis of NPs from the binary metal oxide ceramics supports the successful production of hybrid NPs. Ta, W, and Bi were incorporated in the NPs, which is unlike most traditional chemical synthesis methods, where the metal oxides are bonded on the surface of iron oxide NPs. The crystalline bimetallic NPs synthesized in this work could be further studied for their application as contrast agents.

Declaration of Competing Interest

The authors declare that they have no known competing financial interests or personal relationships that could have appeared to influence the work reported in this paper.

Acknowledgments

This research has been partially funded by the Spanish Ministerio de Ciencia e Innovación through the research project MAT2015- 67354R (MINECO-FEDER). Funding through a Marie Skłodowska-Curie Individual Fellowships (MSCA-IF 2014, 656908-NIMBLIS-ESR) of the Horizon 2020 program, and the Project PI-0030-2017 of the Junta de Andalucía in the framework of the integrated territorial initiative 2014-2020 for research and innovation in biomedicine and health sciences in the province of Cadiz is also greatly appreciated. The authors acknowledge support for scanning electron microscopy by Dr. Stephan Puchegger and the faculty center for nanostructure research at the University of Vienna.

References

[1] V. Amendola, D. Amans, Y. Ishikawa, N. Koshizaki, S. Scirè, G. Compagnini, S. Reichenberger, S. Barcikowski, Room-temperature laser synthesis in liquid of oxide, metal-oxide core-shells, and doped oxide nanoparticles, Chemistry 26 (2020) 9206–9242.
[2] C. Pfeiffer, C. Rehbock, D. Huhn, C. Carrillo-Carrion, D.J. de Aberasturi, V. Merk, S. Barcikowski, W.J. Parak, Interaction of colloidal nanoparticles with their local environment: the (ionic) nanoenvironment around nanoparticles is different from bulk and determines the physico-chemical properties of the nanoparticles, J. R. Soc. Interface 11 (2014) 13.
[3] V. Amendola, M. Meneghetti, Laser ablation synthesis in solution and size manipulation of noble metal nanoparticles, Phys. Chem. Chem. Phys. 11 (2009) 3805–3821.
[4] S. Reichenberger, G. Marzun, M. Muhler, S. Barcikowski, Perspective of surfactant-free colloidal nanoparticles in heterogeneous catalysis, ChemCatChem 11 (2019) 4489–4518.
[5] K. Loza, M. Heggen, M. Epple, Synthesis, structure, properties, and applications of bimetallic nanoparticles of noble metals, Adv. Funct. Mater. 30 (2020) 14.
[6] A.I. Frenkel, Applications of extended X-ray absorption fine-structure spectroscopy to studies of bimetallic nanoparticle catalysts, Chem. Soc. Rev. 41 (2012) 8163–8178.
[7] M.S. Wong, P.J.J. Alvarez, Y.L. Fang, N. Akcin, M.O. Nutt, J.T. Miller, K.N. Heck, Cleaner water using bimetallic nanoparticle catalysts, J. Chem. Technol. Biotechnol. 84 (2009) 158–166.
[8] W. Cao, Y. Liu, F. Xu, Q. Xia, G. Du, Z. Fan, N. Chen, Metal-organic framework derived carbon-coated spherical bimetallic nickel-cobalt sulfide nanoparticles for hybrid supercapacitors, Electrochim. Acta 385 (2021) 138433.
[9] W. Liao, K. Liu, Y. Chen, J. Hu, Y. Gan, Au–Ag bimetallic nanoparticles decorated silicon nanowires with fixed and dynamic hot spots for ultrasensitive 3D SERS sensing, J. Alloys Compd. 868 (2021) 159136.
[10] R. Mandal, A. Baranwal, A. Srivastava, P. Chandra, Evolving trends in bio/chemical sensor fabrication incorporating bimetallic nanoparticles, Biosens. Bioelectron. 117 (2018) 546–561.
[11] Y. Hao, Y. Jiang, L. Zhao, Z. Ye, Z. Wang, D. Chu, F. Wu, L. Li, M. Xie, R. Chen, Bimetallic antimony–vanadium oxide nanoparticles embedded in graphene for stable lithium and sodium storage, ACS Appl. Mater. Interfaces 13 (2021) 21127–21137.
[12] N. Yusoff, A. Pandikumar, R. Ramaraj, H.N. Lim, N.M. Huang, Gold nanoparticle based optical and electrochemical sensing of dopamine, Microchim. Acta 182 (2015) 2091–2114.
[13] A. Tymoczko, M. Kamp, C. Rehbock, L. Kienle, E. Cattaruzza, S. Barcikowski, V. Amendola, One-step synthesis of Fe–Au core–shell magnetic-plasmonic nanoparticles driven by interface energy minimization, Nanoscale Horizons 4 (2019) 1326–1332.
[14] O. Długosz, M. Sochocka, M. Ochnik, M. Banach, Metal and bimetallic nanoparticles: flow synthesis, bioactivity and toxicity, J. Colloid Interface Sci. 586 (2021) 807–818.
[15] Y. Xiang, X. Peng, X. Kong, Z. Tang, H. Quan, Biocompatible AuPd@PVP core-shell nanoparticles for enhancement of radiosensitivity and photothermal cancer therapy, Colloid. Surface. Physicochem. Eng. Aspect. 594 (2020) 124652.
[16] M. Shilo, T. Reuveni, M. Motiei, P. R, Nanoparticles as computed tomography contrast agents: current status and future perspectives, Nanomedicine 7 (2012) 257–269.
[17] M.D. Schnall, Breast imaging technology Application of magnetic resonance imaging to early detection of breast cancer, Breast Canc. Res. 3 (2000) 17.
[18] C. Núñez, S.V. Estévez, M. del, Pilar Chantada, Inorganic nanoparticles in diagnosis and treatment of breast cancer, JBIC Journal of Biological Inorganic Chemistry 23 (2018) 331–345.
[19] M.V. Yezhelyev, X. Gao, Y. Xing, A. Al-Hajj, S. Nie, R.M. O'Regan, Emerging use of nanoparticles in diagnosis and treatment of breast cancer, Lancet Oncol. 7 (2006) 657–667.
[20] M. Wang, M. Thanou, Targeting nanoparticles to cancer, Pharmacol. Res. 62 (2010) 90–99.
[21] N. Yodsanit, B.W. Wang, Y. Zhao, L.W. Guo, K.C. Kent, S.Q. Gong, Recent progress on nanoparticles for targeted aneurysm treatment and imaging, Biomaterials 265 (2021) 15.
[22] Y. Wang, Y. Miao, G. Li, M. Su, X. Chen, H. Zhang, Y. Zhang, W. Jiao, Y. He, J. Yi, X. Liu, H. Fan, Engineering ferrite nanoparticles with enhanced magnetic response for advanced biomedical applications, Mater. Today Adv. 8 (2020) 16.
[23] R.Q. Yin, X.C. Zhang, J.X. Ge, L. Wen, L. Chen, J.F. Zeng, Z. Li, M.Y. Gao, Recent advances in renal clearable inorganic nanoparticles for cancer diagnosis, Part. Part. Syst. Char. (2021) 17, https://doi.org/10.1002/ppsc.202000270.
[24] V. Amendola, A. Guadagnini, S. Agnoli, D. Badocco, P. Pastore, G. Fracasso, M. Gerosa, F. Vurro, A. Busato, P. Marzola, Polymer-coated silver-iron nanoparticles as efficient and biodegradable MRI contrast agents, J. Colloid Interface Sci. 596 (2021) 332–341.
[25] S. Zhao, X. Yu, Y. Qian, W. Chen, J. Shen, Multifunctional magnetic iron oxide nanoparticles: an advanced platform for cancer theranostics, Theranostics 10 (2020) 6278–6309.
[26] M. Carril, I. Fernández, J. Rodríguez, I. García, S. Penadés, Gold-coated iron oxide glyconanoparticles for MRI, CT, and US multimodal imaging, Part. Part. Syst. Char. 31 (2014) 81–87.
[27] I.C. Chiang, C. Dong-Hwang, Structural characterization and self-assembly into superlattices of iron oxide–gold core–shell nanoparticles synthesized via a high-temperature organometallic route, Nanotechnology 20 (2009), 015602.
[28] C. Hoskins, Y. Min, M. Gueorguieva, C. McDougall, A. Volovick, P. Prentice, Z. Wang, A. Melzer, A. Cuschieri, L.J.J.o.N. Wang, Hybrid Gold-Iron Oxide Nanoparticles as a Multifunctional Platform for Biomedical Application, vol. 10, 2012, p. 27.
[29] M.A. Laguna-Marco, C. Piquer, A.G. Roca, R. Boada, M. Andrés-Vergés, S. Veintemillas-Verdaguer, C.J. Serna, A. Iadecola, J. Chaboy, Structural determination of Bi-doped magnetite multifunctional nanoparticles for contrast imaging, Phys. Chem. Chem. Phys. 16 (2014) 18301–18310.
[30] M. Andres-Verges, M.D. Morales, S. Veintemillas-Verdaguer, F.J. Palomares, C. J. Serna, Core/shell magnetite/bismuth oxide nanocrystals with tunable size, colloidal, and magnetic properties, Chem. Mater. 24 (2012) 319–324.
[31] M.A. Koten, M. Pinaki, S.J. E, Core–shell nanoparticles driven by surface energy differences in the Co–Ag, W–Fe, and Mo–Co systems, Part. Part. Syst. Char. 32 (2015) 848–853.
[32] L. Lebron-Zapata, M.S. Jochelson, Overview of breast cancer screening and diagnosis, Pet. Clin. 13 (2018) 301–323.
[33] M.A. Brown, R.C. Semelka, MRI Basic Priciple and Applications, Wiley, 2003.
[34] J. Lee, E. Halpern, E. Rafferty, G. Gazelle, Evaluating the correlation between film mammography and MRI for screening women with increased breast cancer risk, Acad. Radiol. 16 (2009) 1323–1328.
[35] J. Lodhia, G. Mandarano, N. Ferris, P. Eu, S. Cowell, Development and use of iron oxide nanoparticles (Part 1): synthesis of iron oxide nanoparticles for MRI, Biomed. Imaging Interv. J. 6 (2010) 1–11.
[36] W. Wu, Z. Wu, T. Yu, C. Jiang, W. Kim, Recent progress on magnetic iron oxide nanoparticles: synthesis, surface functional strategies and biomedical applications, Sci. Technol. Adv. Mater. 16 (2015), 023501.
[37] K. Hola, Z. Markova, G. Zoppellaro, J. Tucek, R. Zboril, Tailored functionalization of iron oxide nanoparticles for MRI, drug delivery, magnetic separation and immobilization of biosubstances, Biotechnol. Adv. 33 (2015) 1162–1176.
[38] A.K. Gupta, M. Gupta, Synthesis and surface engineering of iron oxide nanoparticles for biomedical applications, Biomaterials 26 (2005) 3995–4021.
[39] A.S. Wahajuddin, Superparamagnetic iron oxide nanoparticles: magnetic nanoplatforms as drug carriers, Int. J. Nanomed. 7 (2012) 3445–3471.
[40] M. Ahmed, M. Douek, The role of magnetic nanoparticles in the localization and treatment of breast cancer, BioMed Res. Int. 2013 (2013) 11.
[41] L. Rueda-Gensini, J. Cifuentes, M.C. Castellanos, P.R. Puentes, J.A. Serna, C. Munoz-Camargo, J.C. Cruz, Tailoring iron oxide nanoparticles for efficient cellular internalization and endosomal escape, Nanomaterials 10 (2020) 56.
[42] M. Bouché, J.C. Hsu, Y.C. Dong, J. Kim, K. Taing, D.P. Cormode, Recent advances in molecular imaging with gold nanoparticles, Bioconjugate Chem. 31 (2020) 303–314.
[43] C. Xu, G.A. Tung, S. Sun, Size and concentration effect of gold nanoparticles on X-ray attenuation as measured on computed tomography, Chem. Mater. 20 (2008) 4167–4169.
[44] K. Ai, Y. Liu, J. Liu, Q. Yuan, Y. He, L. Lu, Large-scale synthesis of Bi2S3 nanodots as a contrast agent for in vivo X-ray computed tomography, Imaging 23 (2011) 4886–4891.
[45] A. Ghazanfari, S. Marasini, X. Miao, J.A. Park, K.-H. Jung, M.Y. Ahmad, H. Yue, S. L. Ho, S. Liu, Y.J. Jang, K.S. Chae, Y. Chang, G.H. Lee, Synthesis, characterization, and X-ray attenuation properties of polyacrylic acid-coated ultrasmall heavy metal oxide (Bi2O3, Yb2O3, NaTaO3, Dy2O3, and Gd2O3) nanoparticles as potential CT contrast agents, Colloid. Surface. Physicochem. Eng. Aspect. 576 (2019) 73–81.
[46] A. Jakhmola, N. Anton, H. Anton, N. Messaddeq, F. Hallouard, A. Klymchenko, Y. Mely, T.F. Vandamme, Poly-ε-caprolactone tungsten oxide nanoparticles as a contrast agent for X-ray computed tomography, Biomaterials 35 (2014) 2981–2986.
[47] J.P.J. Bonitatibus, A.S. Torres, G.D. Goddard, P.F. FitzGerald, A.M. Kulkarni, Synthesis, characterization, and computed tomography imaging of a tantalum oxide nanoparticle imaging agent, Chem. Commun. 46 (2010) 8956–8958.
[48] Y. Liu, K. Ai, J. Liu, Q. Yuan, Y. He, L. Lu, A high-performance ytterbium-based nanoparticulate contrast agent for in vivo X-ray computed tomography imaging, Angew. Chem. 51 (2012) 1437–1442.
[49] T. Nowak, M. Hupfer, R. Brauweiler, F. Eisa, W.A. Kalender, Potential of high-Z contrast agents in clinical contrast-enhanced computed tomography, Med. Phys. 38 (2011) 6469–6482.
[50] H. Lusic, M.W. Grinstaff, X-ray computed tomography contrast agents, Chem. Rev. 113 (2013), https://doi.org/10.1021/cr200358s.

[51] P.C. Naha, A. Al Zaki, E. Hecht, M. Chorny, P. Chhour, E. Blankemeyer, D.M. Yates, W.R.T. Witschey, H.I. Litt, A. Tsourkas, D.P. Cormode, Dextran coated bismuth–iron oxide nanohybrid contrast agents for computed tomography and magnetic resonance imaging, J. Mater. Chem. B 2 (2014) 8239–8248.

[52] H.Y. Lin, W.Y. Chen, Y.C. Chen, Iron oxide/tantalum oxide core-shell magnetic nanoparticle-based microwave-assisted extraction for phosphopeptide enrichment from complex samples for MALDI MS analysis, Anal. Bioanal. Chem. 394 (2009) 2129–2136.

[53] P. Debbage, W. Jaschke, Molecular imaging with nanoparticles: giant roles for dwarf actors, Histochem. Cell Biol. 130 (2008) 845–875.

[54] V. Amendola, M. Meneghetti, What controls the composition and the structure of nanomaterials generated by laser ablation in liquid solution? Phys. Chem. Chem. Phys. 15 (2013) 3027–3046.

[55] J.-W. Park, J.S. Shumaker-Parry, Strong resistance of citrate anions on metal nanoparticles to desorption under thiol functionalization, ACS Nano 9 (2015) 1665–1682.

[56] D. Zhang, B. Gökce, S. Barcikowski, Laser synthesis and processing of colloids: fundamentals and applications, Chem. Rev. 117 (2017) 3990–4103.

[57] H. Zeng, X.-W. Du, S.C. Singh, S.A. Kulinich, S. Yang, J. He, W. Cai, Nanomaterials via laser ablation/irradiation in liquid, Review 22 (2012) 1333–1353.

[58] V. Amendola, S. Barcikowski, A quarter-century of nanoparticle generation by lasers in liquids: where are we now, and what's next? J. Colloid Interface Sci. 489 (2017) 1–2.

[59] A.A. Milner, K. Zhang, Y. Prior, Floating tip nanolithography, Nano Lett. 8 (2008) 2017–2022.

[60] F. Waag, Y. Li, A.R. Ziefuß, E. Bertin, M. Kamp, V. Duppel, G. Marzun, L. Kienle, S. Barcikowski, B. Gökce, Kinetically-controlled laser-synthesis of colloidal high-entropy alloy nanoparticles, RSC Adv. 9 (2019) 18547–18558.

[61] V. Amendola, S. Scaramuzza, F. Carraro, E. Cattaruzza, Formation of alloy nanoparticles by laser ablation of Au/Fe multilayer films in liquid environment, J. Colloid Interface Sci. 489 (2017) 18–27.

[62] C.-Y. Shih, R. Streubel, J. Heberle, A. Letzel, M.V. Shugaev, C. Wu, M. Schmidt, B. Gokce, S. Barcikowski, L.V. Zhigilei, Two mechanisms of nanoparticle generation in picosecond laser ablation in liquids: the origin of the bimodal size distribution, Nanoscale (2018), https://doi.org/10.1039/C7NR08614H.

[63] C.-Y. Shih, M.V. Shugaev, C. Wu, L.V. Zhigilei, The effect of pulse duration on nanoparticle generation in pulsed laser ablation in liquids: insights from large-scale atomistic simulations, Phys. Chem. Chem. Phys. 22 (2020) 7077–7099.

[64] R. Lahoz, A. Naghilou, W. Kautek, O. Bomati-Miguel, Study of the physicochemical surface alterations and incubation phenomena induced on iron targets by nanosecond pulsed laser ablation in liquids: effect on productivity and characteristics of the synthesized nanoscale zero-valent iron (nZVI) particles, Appl. Surf. Sci. 511 (2020) 145438.

[65] R. Lahoz, E. Natividad, Á. Mayoral, C. Rentenberger, D. Díaz-Fernández, E.J. Félix, L. Soriano, W. Kautek, O. Bomati-Miguel, Pursuit of optimal synthetic conditions for obtaining colloidal zero-valent iron nanoparticles by scanning pulsed laser ablation in liquids, J. Ind. Eng. Chem. 81 (2020) 340–351.

[66] S. Ibrahimkutty, P. Wagener, A. Menzel, A. Plech, S. Barcikowski, Nanoparticle formation in a cavitation bubble after pulsed laser ablation in liquid studied with high time resolution small angle x-ray scattering 101 (2012) 103104.

[67] M. Dell'Aglio, A. Santagata, G. Valenza, A. DeStradis, A. DeGiacomo, Study of the effect of water pressure on plasma and cavitation bubble induced by pulsed laser ablation in liquid of silver and missed variations of observable nanoparticle, Features 18 (2017) 1165–1174.

[68] N. Lasemi, U. Pacher, C. Rentenberger, O. Bomatí-Miguel, W. Kautek, Laser-Assisted synthesis of colloidal Ni/NiOx core/shell nanoparticles in water and alcoholic solvents, ChemPhysChem 18 (2017) 1118–1124.

[69] N. Lasemi, O. BomatíMiguel, R. Lahoz, V.V. Lennikov, U. Pacher, C. Rentenberger, W. Kautek, Laser-Assisted synthesis of colloidal FeWxOy and Fe/FexOy nanoparticles in water and ethanol, ChemPhysChem 19 (2018) 1414–1419.

[70] H. Kleykamp, Zur thermodynamik in den systemen Fe-W, Fe-W-O und Fe-W-C, J. Less Common Met. 71 (1980) 127–134.

[71] R.S. Roth, J.L. Waring, W.S. Brower, Effect of oxide additions on the polymorphism of tantalum pentoxide, JOURNAL OF RESEARCH of the Notional Bureau of Standards - A 74 (1970) 477–484.

[72] K. Kitayama, Experimental study of equilibria in the Ta_2O_5-Fe-Fe_2O_3 system at 1200°C, J. Solid State Chem. 64 (1986) 162–168.

[73] E.I. Speranskaya, V.M. Skorikov, E.Y. Rode, V.A. Terekhova, Bismuth oxide–iron (III) oxide phase diagram, Izvestiya Akad. Nauk SSSR Seriya Khim. 5 (1965) 905–906.

[74] E.I. Speranskaya, V.M. Skorikov, E.Y. Rode, V.A. Terekhova, The phase diagram of the system bismuth oxide-ferric oxide, Bulletin of the Academy of Sciences of the USSR, Division of chemical science 14 (1965) 873–874.

[75] O. Armbruster, A. Naghilou, H. Pöhl, W. Kautek, In-situ and non-destructive focus determination device for high-precision laser applications, J. Opt. 18 (2016), 095401.

[76] A. Angheluta, C. Mihesan, F. Doroftei, A. Dascalu, L. Ursu, M. Velegrakis, M. Pinteala, Formation by laser ablation in liquid (LAL) and characterization of citric acid-coated iron oxide nanoparticles, Rev. Roum. Chem. 59 (2014) 151–159.

[77] J. Liu, Simple technique for measurements of pulsed Gaussian-beam spot sizes, Opt Lett. 7 (1982) 196–198.

[78] J. Krüger, W. Kautek, Ultrashort pulse laser interaction with dielectrics and polymers, Adv. Polym. Sci. 168 (2004) 247–290.

[79] J.M. Khosrofian, B.A. Garetz, Measurement of a Gaussian laser beam diameter through the direct inversion of knife-edge data, Appl. Opt. 22 (1983) 3406–3410.

[80] J. Schiemer, M.A. Carpenter, D.M. Evans, J.M. Gregg, A. Schilling, M. Arredondo, M. Alexe, D. Sanchez, N. Ortega, R.S. Katiyar, M. Echizen, E. Colliver, S. Dutton, J. F. Scott, Studies of the room-temperature multiferroic Pb $(Fe_{0.5}Ta_{0.5})_{0.4}(Zr_{0.53}Ti_{0.47})_{0.6}O_3$: resonant ultrasound spectroscopy, dielectric, and magnetic phenomena, Adv. Funct. Mater. 24 (2014) 2993–3002.

[81] M.C. Ortega-Liébana, J.L. Hueso, R. Arenal, R. Lahoz, G.F. de la Fuente, J. Santamaría, Continuous-mode laser ablation at the solid–liquid interface of pelletized low-cost materials for the production of luminescent silicon carbide nanocrystals, J. Phys. Chem. C 119 (2015) 2158–2165.

[82] A. Yanguas-Gil, J.L. Hueso, J. Cotrino, A. Caballero, A.R. González-Elipe, Reforming of ethanol in a microwave surface-wave plasma discharge, Appl. Phys. Lett. 85 (2004) 4004–4006.

[83] O. Armbruster, A. Naghilou, W. Kautek, The role of defects in laser-matter interaction, in: M. Dinescu, D.B. Geohegan, A. Miotello, P.M. Ossi (Eds.), Advances in the Application of Lasers in Materials Science 274, Springer Series in Materials Science, Springer, Cham, 2018, https://doi.org/10.1007/978-3-319-96845-2.

[84] A. Naghilou, O. Armbruster, M. Kitzler, W. Kautek, Merging spot size and pulse number dependence of femtosecond laser ablation thresholds: modeling and demonstration with high impact polystyrene, J. Phys. Chem. C 119 (2015) 22992–22998.

[85] M.V. Shugaev, C. Wu, O. Armbruster, A. Naghilou, N. Brouwer, D.S. Ivanov, T.J.-Y. Derrien, N.M. Bulgakova, W. Kautek, B. Rethfeld, L.V. Zhigilei, Fundamentals of ultrafast laser-material interaction, MRS Bull. 42 (2016) 960–968.

[86] O. Armbruster, A. Naghilou, M. Kitzler, W. Kautek, Spot size and pulse number dependence of femtosecond laser ablation thresholds of silicon and stainless steel, Appl. Surf. Sci. 396 (2017) 1736–1740.

[87] A. Naghilou, O. Armbruster, W. Kautek, Femto- and nanosecond pulse laser ablation dependence on irradiation area: the role of defects in metals and semiconductors, Appl. Surf. Sci. 418 (2017) 487–490.

[88] M. Reichling, A. Bodemann, N. Kaiser, Defect induced laser damage in oxide multilayer coatings for 248 nm, Thin Solid Films 320 (1998) 264–279.

[89] Y.-w. Jun, Y.-M. Huh, J.-s. Choi, J.-H. Lee, H.-T. Song, S. Kim, S. Yoon, K.-S. Kim, J.-S. Shin, J.-S. Suh, J. Cheon, Nanoscale size effect of magnetic nanocrystals and their utilization for cancer diagnosis via magnetic resonance imaging, J. Am. Chem. Soc. 127 (2005) 5732–5733.

[90] Z. Cai, C. Wu, L. Yang, D. Wang, H. Ai, Assembly-controlled magnetic nanoparticle clusters as MRI contrast agents, ACS Biomater. Sci. Eng. 6 (2020) 2533–2542.

[91] P. Pouli, D.C. Emmony, C.E. Madden, I. Sutherland, Analysis of the laser-induced reduction mechanisms of medieval pigments, Appl. Surf. Sci. 173 (2001) 252–261.

[92] S. Arif, W. Kautek, Laser cleaning of particulates from paper: comparison between sized ground wood cellulose and pure cellulose, Appl. Surf. Sci. 276 (2013) 53–61.

[93] N. Lasemi, U. Pacher, L.V. Zhigilei, O. Bomatí-Miguel, W. Kautek, Pulsed laser ablation and incubation of nickel, iron and tungsten in liquids and air, Appl. Surf. Sci. 433 (2018) 772–779.